ADVANCED MATERIALS INTERFACES
www.advmatinterfaces.de



# Surface Oxidation as a Cause of High Open-Circuit Voltage in CdSe ETA Solar Cells

*Saar Kirmayer,* Eran Edri, Douglas Hines, Nir Klein-Kedem, Hagai Cohen, Olivia Niitsoo, Iddo Pinkas, Prashant V. Kamat, and Gary Hodes**

**$TiO_2$/CdSe/CuSCN extremely thin absorber (ETA) solar cells are found to give relatively high values of open-circuit voltage (>0.8 V) but low currents upon annealing the cadmium selenide (CdSe) in air (500 °C). Annealing in $N_2$ produces much lower photovoltages and slightly lower photocurrents. Band structure measurements show differences between the two annealing regimes that, however, appear to favor the $N_2$-annealed CdSe. On the other hand, chemically resolved electrical measurements (CREM) of the cells reveal marked differences in photo-induced charge trapping, in particular at absorber grain boundaries of the air versus $N_2$-annealed systems, correlated with the formation of Cd–O species at the CdSe surface. Using transient absorption and photovoltage decay, pronounced lifetime differences are also observed, in agreement with the strong suppression of charge recombination. The results point to a multiple role of grain surface-oxidation, which both impedes electron injection from the CdSe to the $TiO_2$, but, much more significantly, enhances hole injection to the CuSCN via passivation of hole traps that act as efficient recombination centers.**

## 1. Introduction

Cadmium selenide (CdSe) is a commonly used absorber material in thin-film solar cells because of its ease of preparation by solution methods together with its bulk bandgap of 1.73 eV that allows the harvesting of visible photons quite effectively. It has been commonly studied for photoelectrochemical (PEC) cells, both as thin films in the 1970s and 1980s, and more recently as a sensitizer in semiconductor-sensitized solar cells (SSSCs).[1] Many different solution methods have been developed for CdSe (and other semiconductors) deposition, most common of which are chemical bath deposition (CBD),[2,3] successive ionic layer and reaction (SILAR),[4–7] electrodeposition (ED),[8–10] electrophoresis, and adsorption or chemical linking of colloids.[1,11–13]

Although CdSe has been the popular choice for liquid junction solar cells, it is not being explored extensively in all-solid-state solar cells. The simplest configuration for such cells is the metal–semiconductor Schottky cell[14,15] Bulk heterojunction cells with CdSe nanoparticles blended with a conjugated polymer and cast on a transparent electrode have been employed.[16–20] Another convenient approach employs the use of an extremely thin absorber (ETA) cell, where CdSe is deposited into a mesoporous oxide with a solid-hole conductor infiltrated into the porous structure.[6,8,21–25] In an ETA cell, a very thin layer of inorganic semiconductor absorber (a few nanometers to a few tens of nanometers) is deposited onto a mesoporous electron acceptor, usually $TiO_2$ or ZnO. Upon light absorption in the CdSe, electrons are injected into the $TiO_2$ while holes are collected by a hole conductor intercalated throughout the film and transported to the back electrode.

The early CdSe-based cells were PEC cells based on either single crystals or thin films of CdSe in polysulfide electrolyte.[26] Open-circuit voltage ($V_{OC}$) values typically ranged between 0.5 and 0.7 V. A few examples in the literature reported voltages exceeding 0.7 V, particularly evident for single crystal CdSe 0.76 [27] and 0.82 V.[28] The $V_{OC}$ of nanostructured CdSe-based liquid junction SSSCs are somewhat lower; typically exhibiting values between 0.5 and 0.6 V. Many of these cells employ CdSe quantum dots (QDs), with higher than bulk bandgap and therefore their $V_{OC}$ should not be directly compared with that of cells using bulk CdSe. Having lower $V_{OC}$ for SSSCs compared to (nonsensitized) PECs is not surprising, considering the additional voltage loss that is expected at the CdSe-porous oxide interface.

Turning to solid-state cells, the older literature describes Schottky cells with $V_{OC}$ values of 0.65[14] and 0.72 V.[15] The more modern solid-state cells can be divided into two types: nanoparticle CdSe in a blend with conjugated polymers and ETA cells. The former is more common and corresponding $V_{OC}$ reports

Dr. S. Kirmayer, E. Edri, N. Klein-Kedem,
Dr. O. Niitsoo,[+] Prof. G. Hodes
Department of Materials and Interfaces
Weizmann Institute of Science
Rehovot 76100, Israel
E-mail: saar.kirmayer@weizmann.ac.il;
gary.hodes@weizmann.ac.il

D. Hines, Prof. P. V. Kamat
Radiation Laboratory
Department of Chemical & Biomolecular Engineering
and Department of Chemistry & Biochemistry
University of Notre Dame
Notre Dame, Indiana 46556, USA

Dr. H. Cohen, Dr. I. Pinkas
Department of Chemical Research Support
Weizmann Institute of Science
Rehovot 76100, Israel

[+]*Present address*: Advenira Enterprises, Inc., Sunnyvale, California 94085, USA

**DOI: 10.1002/admi.201400346**

  

vary considerably. Considering only those that give particularly high $V_{OC}$ values (>0.7 V), we find three examples: 0.76 ,[29] 0.95, [20] and 1.0 V.[30]. In all these three studies, the CdSe was size quantized, either to a relatively small degree[20,30] with bandgaps between 1.85 and 1.9 eV, or to a moderate degree[29] with estimated bandgap of ca. 2 eV. There are relatively few CdSe-based ETA cells—the subject of this paper—reported in the literature, probably because their efficiency has not been particularly promising in most cases. Table S1 (the Supporting Information) shows the relevant data for published CdSe-based ETA cells. The highest $V_{OC}$ for nonquantized CdSe (to compare with our results in this paper) is 0.59 V (and 0.7 V for a moderately quantized—1.9 eV bandgap) cell. There is indeed some basic correlation between bandgap and $V_{OC}$, since $V_{OC}$ will always be less than the bandgap (in the absence of a successful hot electron cell). However, even more relevant for this paper is the inverse correlation found between $V_{OC}$ and short circuit current ($I_{SC}$) in Table S1 (Supporting Information). This is not simply due to less light absorption in a higher bandgap material; the differences in $I_{SC}$ are much too large for this to be the main reason.

In this paper, we show high values of $V_{OC}$ (up to 0.84 V) in $TiO_2$/CdSe (nonquantized)/CuSCN ETA cells, which are associated with rather low values of $I_{SC}$ (up to ca. 3.3 mA $cm^{-2}$). We show how both the elevated voltage and the reduced currents are caused by CdSe-surface oxidation that is formed upon air annealing. This oxidation greatly suppresses the electron/hole recombination rate. The voltage increase can also be explained by changes in the energy-band alignments across cell interfaces, which play an important role upon illumination. The relatively low photocurrent obtained, while still higher than those of the $N_2$-annealed samples, may be limited in part by a small offset (therefore a small driving force) measured between the $TiO_2$ and the CdSe conduction bands (CB). Fast recombination in the CdSe is the main loss mechanism for the $N_2$-annealed (nonoxidized) samples.

## 2. Results and Discussion

### 2.1. Basic Structural and Optical Characterization

The basic structure of the ETA solar cell discussed in this work is schematically drawn in **Figure 1**a as well as demonstrated in the SEM cross section of a half cell (without the hole conductor) in Figure 1b. The fluorine-doped tin oxide (FTO)-coated glass is covered with a dense ca. 100-nm-thick $TiO_2$ layer (appears as a continuous darker layer on top of the bright FTO layer at the left-hand side of Figure 1b). The as-deposited CdSe forms particles of ca. 4 nm (Figure 1c) within the 3–4 μm thick mesoscopic $TiO_2$ layer. On annealing, these nanoparticles exhibit sizes typically around 100 nm in diameter and are visible as brighter dots well dispersed within the film (Figure 1b). Additional formation of CdSe clusters on top of the mesoporous $TiO_2$ film (the darker ca. 20% top part of the tilted cross section) is also seen. This layer, typically of 100 nm in width, exhibits a more irregular shape. The solar cell is then configured following infiltration of the hole conductor to fill the voids in the mesoporous $TiO_2$–CdSe network and evaporated gold contact.

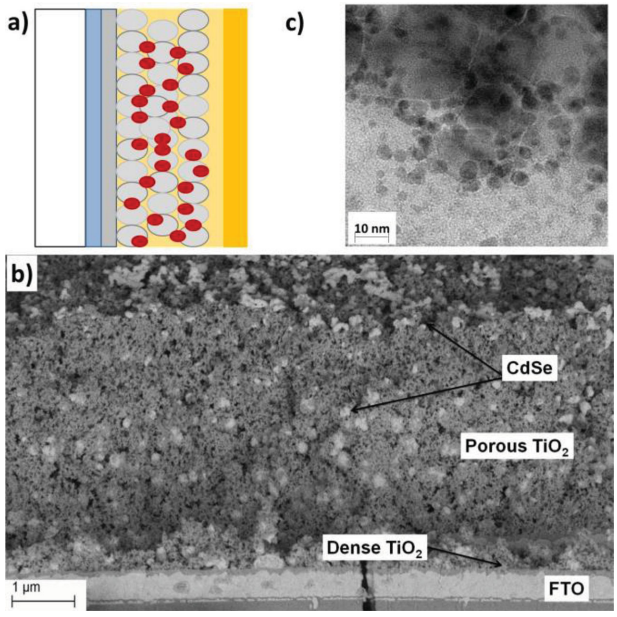


**Figure 1.** a) Schematic of the cell structure (from left to right). Glass substrate, FTO, thin dense $TiO_2$ layer, mesoporous $TiO_2$ with CdSe, CuSCN hole conductor, and gold contact. b) Back-scattered electron-tilted cross-section image of a cell after annealing the CdSe at 500 °C in air. The darker top ca. 20% of the image shows the top part of the film. c) TEM image of as-deposited CdSe nanoparticles on 25-nm $TiO_2$ particles.

The X-ray diffraction (XRD) pattern of as-deposited CdSe on fluorine-doped tin oxide, as shown in Figure S1 (Supporting Information), was analyzed to give a domain size of ca. 4 nm in agreement with earlier studies.[31,32] Upon annealing, the crystal size grows to about 50 nm at 500 ºC and a well-known cubic-to-hexagonal transition occurs starting at ca. 300 ºC (see the Supporting Information for more detail).

The optical properties of these electrodeposited-CdSe films have already been described in detail in refs.[31] and [32] Transmission spectra of the as-deposited and annealed (500 ºC in air) films on nanoporous $TiO_2$ are given in Figure S2 (Supporting Information). They show similar features to those already described in refs. [31] and [32]. For the annealed film, the inflection point at ca. 700 nm and slow decrease in transmission toward shorter wavelengths show that the film is thin (estimated roughly 150-nm optical thickness) and therefore does not absorb all the supra-bandgap light. However, we find that appreciably thicker films give poorer photocurrents.

### 2.2. Complete Cells

**Figure 2** shows *J–V* characteristics of cells made from CdSe/$TiO_2$ films as-deposited and air-annealed at various temperatures. While the cell made using the as-deposited CdSe shows poor performance with $V_{OC}$ of ca. 450 mV and $J_{SC}$ ca. 20 μA $cm^{-2}$, upon annealing in air, the cell performance improves dramatically with an optimal annealing temperature of 450–500 ºC. Typically for such annealed films, $V_{OC}$ ranges between 0.70 and 0.85 V and $J_{SC}$ typically yields 1–2 mA $cm^{-2}$ (best value, 3.3 mA $cm^{-2}$). While the values of $J_{SC}$

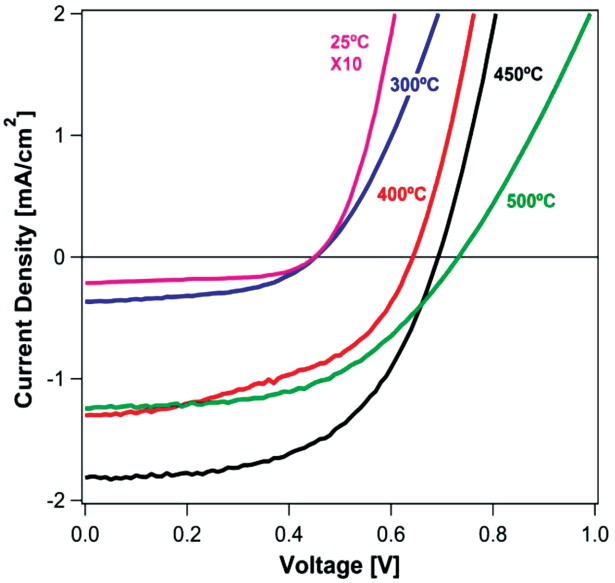


**Figure 2.** Photocurrent density versus voltage curves of FTO/$TiO_2$/CdSe/CuSCN/Au solar cells employing CdSe/$TiO_2$ films annealed at different temperatures in air. All devices are 1.1 cm$^2$. Illumination was AM1.5 100 mW cm$^{-2}$. Dark curves are shown in Figure S3.

vary considerably from one cell to another, the trends shown here are consistent. Cells that were annealed appreciably above 500 °C deteriorated, possibly due to excessive oxidation and/or surface melting of the glass substrate.

The improvement in performance with annealing up to 450 °C could be attributed to the increase in crystal size or to the improvement in crystal quality. Both of these are expected to suppress electron/hole recombination in the CdSe, due to the reduced role of grain boundaries and crystal defects. However, comparison of the annealing effect in air and in nitrogen (**Figure 3**a,b) shows that neither of these factors can explain the improvement in $V_{OC}$ under annealing in air. Annealing in either $N_2$ or air is expected to increase the crystal size and its quality in a similar manner. Indeed, annealing in $N_2$ has the same effect on crystal size as annealing in air (Figure 3a,b). However, while $N_2$ annealing typically causes a moderate improvement in $J_{SC}$, it shows essentially no effect on $V_{OC}$, compared with as-deposited samples.

### 2.3. Band Structures of Partial and Full Solar Cells—Comparison of Air and $N_2$ Annealing of CdSe

A more detailed understanding of the chemical and electrical properties of the samples is obtained by X-ray photoelectron spectroscopy (XPS) and chemically resolved electrical measurements (CREM).[33] The latter provides a powerful probe of energy band positions across the multilayer heterostructure, with all beam-induced electrostatic changes practically eliminated.[34] Details regarding the extraction and interpretation of signals originated at relatively deep domains are given in the Supporting Information.

Band diagrams, constructed from CREM data, of CdSe/$TiO_2$ half cells as-deposited and air-annealed under different

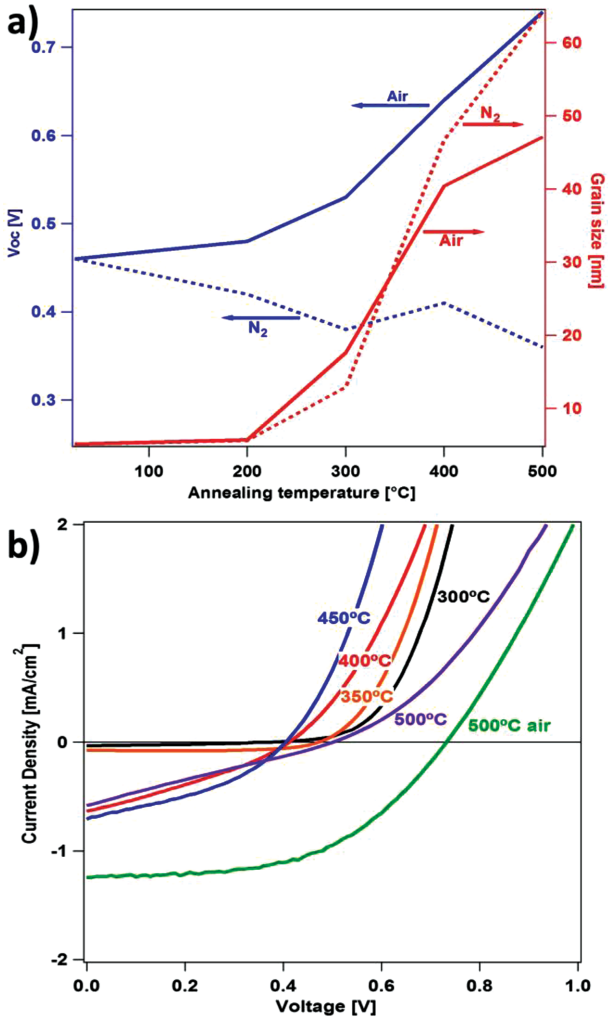


**Figure 3.** a) Variation in open-circuit voltage (blue line—left axis) and grain size (red line—right axis) as a function of annealing temperature in air (solid lines) and $N_2$ (broken lines). b) Current density versus voltage curves for electrodes annealed under nitrogen at variable temperature in comparison to air annealing. Dark curves are shown in Figure S3. The area of all devices is 1.1 cm$^2$.

conditions are shown and discussed in Figure S4 (Supporting Information). The band diagram of the complete solar cell configuration (using air-annealed films), as shown in **Figure 4**, presents a somewhat lower $_{CB}$-offset between the $TiO_2$ and CdSe (0.1 eV), which should still allow electron injection into the $TiO_2$ but with a rather low driving force. There is a large (1.0 eV) offset between the valence-band energies ($E_{VB}$) of CdSe and CuSCN. This offset should be the source of a substantial loss in photovoltage. The full cell with $N_2$-annealed film shows a reduced CB offset (0.5 eV) compared with the situation without the CuSCN (0.8 eV), yet it is much higher than for the cell made from an air-annealed film, as well as the large (yet smaller than for the air-annealed—0.8 eV) $E_{VB}$ offset between the CdSe and CuSCN layers. Thus, the various offsets in both cells do not explain the higher $I_{SC}$ and $V_{OC}$ obtained with the air-annealed films. On the contrary, they would even suggest (based on conduction-band offsets) a higher $I_{SC}$ for the $N_2$-annealed sample.

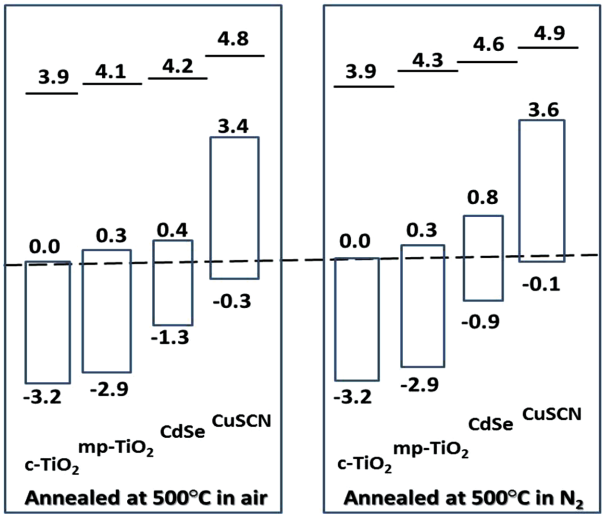


**Figure 4.** Full cell-energy-band alignment for air-annealed (left) and $N_2$-annealed (right) CdSe. Sample structure is FTO/compact $TiO_2$/mesoporous $TiO_2$/CdSe/CuSCN. Note that the sample is connected through the FTO substrate to the XPS spectrometer ground; therefore the Fermi-level position is the reference for all measurements, common to all samples. The local vacuum level can therefore change, such that differences in local vacuum level (= work functions, given by top lines and numbers) between different layers represent internal electric fields. The figure does not differentiate between sharp fields, such as a dipole layer, and fields distributed across macroscopic distances (band slanting) within the relatively thick layers. Numbers are given in eV.

Next, useful information emerges from the inspection of layer-specific photovoltages, as derived from changes in the XPS core-level energies under white light illumination (a relatively weak source, roughly equivalent to 0.1 sun). The corresponding line-shifts of Cu, Cd, Se, Se(O), and Ti are shown in **Figure 5** for $N_2$- and air-annealed samples. For these measurements, the CuSCN was very thin to allow easy detection of all the layers in the cell. In general, a common trend is

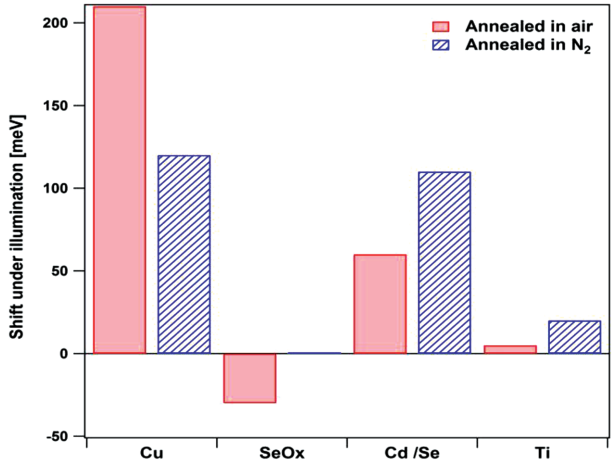


**Figure 5.** A bar diagram showing the shift in core level XPS under low-intensity white-light illumination (< 0.1 sun) of copper (from thin layer of CuSCN), cadmium (from CdSe), and titanium (from $TiO_2$) in cells fabricated from CdSe annealed at 500 °C in air (filled) and $N_2$ (striped). The Se–Ox line-shift in air-annealed samples is shown as well.

seen, where the Cu shift is the largest and the Ti shift is the smallest, as expected from the light-induced charge separation, with the sign and relative magnitudes of line-shifts obeying the stacking order of the layers (note again that the FTO, on which the $TiO_2$ sits, is grounded, which removes most of the negative charge that would otherwise accumulate in the $TiO_2$). However, the magnitudes of these shifts for the two types of annealing conditions lead to an interesting observation. Ideally, if all light-induced holes accumulate at the top CuSCN layer and all corresponding electrons are removed to ground, there should be a monotonic field across the device, expressed in a gradual decrease in the elemental shifts going from Cu to Ti. For the $N_2$-annealed sample, however, the difference between the Cu and Cd(Se) peaks is small. From this observation, we conclude that there is a significant buildup of positive charge at the ($N_2$-annealed) CdSe, other than at the CuSCN, and that this is attributed to efficient hole trapping at the unpassivated CdSe, mainly at its surface Se dangling bonds.

The air-annealed sample does show the expected gradual change in photoshifts from element to element, however, with significantly different magnitude and with the exception of oxidized Se, which undergoes a small but clearly defined negative shift (the other, nonoxidized Se component shifts identically, within experimental error, to the Cd line). Considering for each element, the differences between the two samples in Figure 5, one notes that (1) the positive line-shift of Cu for the air-annealed sample is considerably greater than for the $N_2$-annealed one and (2) in contrast to the former, that the Cd and Ti line-shifts of the air-annealed sample are smaller than those of the $N_2$-annealed one. These results suggest that (1) the positive charge builds up efficiently at the CuSCN of the air-annealed sample and (2) there may even be some net negative charge accumulated in the absorber grains of the latter (clearly seen on the Se–O at least).

Taking into account the lower photocurrents obtained with the $N_2$-annealed samples, we conclude that hole transfer to the CuSCN in the air-annealed sample is facilitated, compared with that in the $N_2$-annealed one, and that the limiting factor in the latter is hole trapping. While charge trapping does not automatically mean poorer charge transfer (in some cases, it could facilitate it, e.g., if there is overlap between the trapped charge and the charge acceptor), in this case, the experimental data strongly indicate that the hole traps act as recombination centers that impede the charge separation in $N_2$-annealed samples. Complementarily, a second, minor effect is inferred from Figure 5: The efficiency of electron evacuation to ground at the air-annealed sample is suppressed, a fact supported by the difference between the two types of annealing in the Cd and Ti line-shifts, Figure 5, and the negative charging seen on the Se–$O_x$ signal.

It is noted that for the $N_2$-annealed sample, as deduced from Figures 4 and 5, the $TiO_2$/CdSe CB offset is reduced under light by ca. 100 meV, which leaves ca. 0.4 eV offset, sufficient for electron injection to the $TiO_2$. On the other hand, for the air-annealed case, the $TiO_2$/CdSe CB offset is reduced to ca. 0.04 eV, which leaves only a very small driving force for electron injection. This fact is in good agreement with the above observation of decreased efficiency in electron evacuation from the absorber grains (lower $J_{SC}$ values), in spite of the removal

**Table 1.** XPS analysis of the surface composition of $TiO_2$/CdSe samples, annealed at different temperatures in air (except for the last sample, which was annealed in $N_2$). All values of O refer to the specific O component associated with the corresponding element (e.g., the O in Ti:O refers only to the resolved component of O bound to Ti). $Se_{red}$ refers to the $Se^{2-}$ component only.

| Annealing temperature | Ti:O | $Se_{OX}$:$Se_{red}$ | Cd:$Se_{total}$ | Cd:$Se_{red}$ | Cd:Ti |
|---|---|---|---|---|---|
| as-deposited | 0.50 | 0.06 | 1.03 | 1.09 | 1.03 |
| 300 °C | 0.47 | 0.32 | 1.37 | 1.81 | 1.31 |
| 400 °C | 0.49 | 0.97 | 1.65 | 3.25 | 1.18 |
| 500 °C | 0.49 | 1.01 | 1.63 | 3.27 | 1.41 |
| 500 °C $N_2$ | 0.56 | 0.00 | 1.27 | 1.27 | 0.84 |

of recombination centers. Yet, the emergence of electron traps, instead of hole traps, at the air-annealed absorber grains, should be considered as well. Thus, the strength of the CREM technique, which allows electrical information to be obtained from selected regions of a sample, is clearly evident in establishing the band structure of CdSe films.

Complementary to the electrical data, the XPS composition analysis provides specific information on the surface species characteristic of the two samples. The complete dataset is presented in Table S2 (Supporting Information) and atomic ratios for the main components are shown in **Table 1**. The ratio between Ti and O, associated with $TiO_x$, (nominally $TiO_2$ but stoichiometry may vary at the surface, where it is being measured) was found within the experimental error to be constant at 1:2 regardless of the annealing temperature. Under increased annealing temperatures (in air), an increase in the Cd to Se ratio, as well as an increase in $SeO_x$:Se and O:Cd, is seen. For comparison, the surface composition of a nitrogen-annealed sample is also given: In this case, no $SeO_x$ is found and the CdSe is more stoichiometric than in the air-annealed (500 °C) sample. The increase in the Cd:Se ratio upon air annealing is commonly associated with loss of $SeO_2$ by sublimation.[35] Accordingly, the Cd:$Se_{red}$ ratio increases upon annealing and the ratio for the air-annealed samples is larger than for the $N_2$-annealed ones. As the $SeO_x$:Se ratio increases with increasing temperature of air annealing, this implies cadmium selenate or selenite forms at the surface, since $SeO_2$ is expected to be increasingly lost at higher temperatures.

From this information, it can be deduced that while $SeO_x$ is formed upon annealing above room temperature, $CdO_x$ is formed only when the temperature is high enough, in this case above 400 °C, and therefore the increase in open-circuit voltage is likely correlated with the formation of these $CdO_x$ species. In support of this conclusion, Ebina et al.[35] noted that oxygen adsorbs ten times faster on the (0001) Se face than on the opposite (0001) Cd face of CdSe crystals and that $SeO_2$ is formed early in the (room temperature but with X-ray and electron-beam irradiation) oxidation and CdO formed only later. A theoretical study has also concluded that Cd-rich surfaces of CdSe quantum dots are passivated (bandgap states removed) by oxygen exposure while for Se-rich surfaces, the effect of oxygen is much smaller with only a partial reduction in surface state density.[36] This may be particularly relevant to our observation that formation of Cd–O, rather than Se–O, is the important process in cell improvement. Cd oxidation can remove Cd dangling bonds that would act as shallow electron traps.[36] Additionally, surface oxidation may passivate the CdSe against Cu substitution from the CuSCN solution.

Thus, air annealing forms a shell around the CdSe core consisting of some oxidized species, and the increase in concentration of these surface species seems to be in good correlation with improved cell performance. The significance of these oxide species at the surface/interface of the CdSe was further corroborated by using the air-annealed CdSe/$TiO_2$ as a photoelectrode in a polysulfide-based liquid junction cell. Once a reasonable performance of the cell was confirmed, the CdSe/$TiO_2$ was rinsed thoroughly with water, dried, and then implemented into a solid-state cell by applying a CuSCN layer followed by Au deposition. The polysulfide converts oxidized Cd species, such as $CdSeO_x$ and CdO to CdS due to the much smaller solubility product ($K_{SP}$) of CdS compared with the other compounds. And indeed, such cells exhibited very poor performance, with very low values of both $V_{OC}$ and $J_{SC}$.

### 2.4. Kinetic Processes

#### *2.4.1. Femtosecond Transient Absorption Analysis*

To determine the effect of the $O_2$ annealing environment on electron-hole recombination dynamics, we employed femtosecond transient absorption spectroscopy. We prepared films of CdSe on alumina and exposed them to $N_2$ and air during the annealing process. (Some results on $TiO_2$ are discussed in Figure S5, Supporting Information). The transient absorption spectrum, **Figure 6**A, is monitored over the course of 1.6 ns after excitation with a 387-nm excitation pulse. Kinetic analyses for these CdSe–$Al_2O_3$ samples were performed at the first-excitonic bleach maximum, ≈720 nm for either annealing environment. The other features in the spectra are briefly explained in the Supporting Information.

Transient absorption kinetic traces were fit to a multiexponential kinetic decay, which revealed three major components contributing to the decay of the excited state (Figure 6b). These processes are summarized in **Table 2**, and correlate well with previously reported time constants for colloidal QDs.[37] Interestingly, the decay for the CdSe–$Al_2O_3$ samples annealed in air show a much slower recovery to the ground state. This result implies that the oxygen-rich environment oxidizes the CdSe surface and passivates recombination sites, which correlates well with conclusions drawn from our XPS/CREM data. This increase in excited-state lifetime of the air-annealed samples would result in significant charge buildup in the electrode system thus, contributing to an increase in $V_{OC}$ during solar cell operation. Note that the CdSe–$Al_2O_3$ films used in this study were prepared via Successive Ion Layer And Reaction (SILAR, which gave comparable values of $V_{OC}$ to the electrodeposited CdSe), as it is not possible to electrodeposit material into an insulating $Al_2O_3$ substrate. The changes seen in excited-state dynamics of CdSe films confirm the suppression of charge recombination in air-annealed samples, which will lead to increases in both photocurrent and photovoltage.

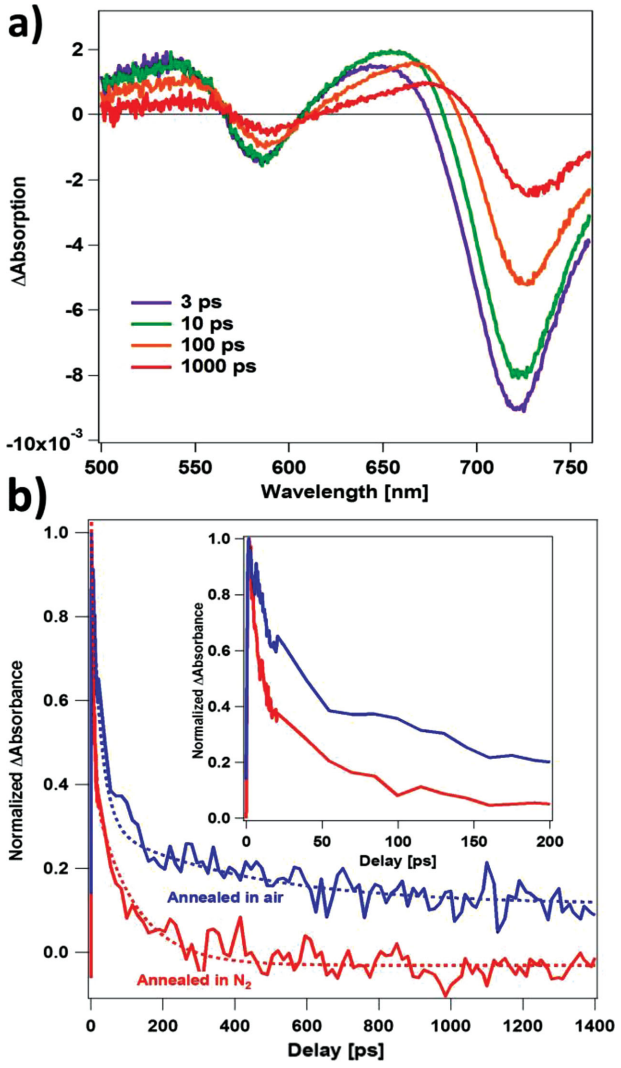


**Figure 6.** a) Transient absorption spectrum of CdSe deposited by SILAR on mesoporous alumina on glass annealed in nitrogen at 500 °C taken at 3 (purple), 10 (green), 100 (orange), and 1000 ps (red). b) Transient absorption decay curves of $N_2$-annealed sample from (a) (red line) CdSe and a similar one but annealed at 500 °C in in air (blue line) probed at 700 nm. The inset shows the same decay curves on a shorter time scale.

*2.4.2. Photovoltage Decay/Charge Extraction*

We measured charge-carrier lifetime as a function of charge-carrier density, normally assumed to be dominated by the $TiO_2$ (thereby, comparing lifetimes at the same charge density) for cells made from air- and $N_2$-annealed CdSe. The change in the decay lifetime at $V_{OC}$ as a function of the charge density at open circuit is shown in **Figure 7**a. In spite of the scatter of the data, particularly for the $N_2$-annealed sample, it is clear that for a given charge density, the air-annealed sample shows about two orders of magnitude larger lifetime. It is possible that the difference is smaller than this, e.g., if recombination is so fast in the $N_2$-annealed case that not all the charge is extracted in the measurement. However, this cannot change the central conclusion. It is usually assumed in such cells that this charge is stored in the $TiO_2$ traps. However, there are other possible locations in our cells where charge can be stored, such as in the CdSe absorber, particularly in the oxidized surface layer, and in the CuSCN.

**Table 2.** Time constants ($\tau$) and fraction of the total signal for the various decay processes in air- and nitrogen-annealed SILAR CdSe grown on alumina.

| | Air | | Nitrogen | |
|---|---|---|---|---|
| Process 1 | 5 ps | 0.01 | 1 ps | 0.43 |
| Process 2 | 15 ps | 0.61 | 4.3 ps | 0.42 |
| Process 3 | 232 ps | 0.38 | 70 ps | 0.15 |

To understand the possible causes of this increase in lifetime, which will favor an increase in both $V_{OC}$ and in photocurrent, we consider four potential recombination mechanisms in this system (**Scheme 1**). Since the photocurrents are relatively low even in the best cases, we expect most of the charges to recombine, with varying degrees of contribution from these processes.

Considering first direct recombination in the CdSe (route 1 in Scheme 1), we have already discussed reduction of this recombination in the oxidized samples based on the TA results and that this passivation correlates with formation of Cd–O species at the CdSe surfaces and interfaces. An increasing charge-carrier lifetime in the absorber means a higher probability for its injection to the relevant carrier conductor. In view of the much lower CB offset and the expected presence of a partially blocking oxidized CdSe layer at the air-annealed $TiO_2$ interface, compared with the $N_2$ interface, the $N_2$-annealed sample is expected to exhibit a faster electron injection rate than the air-annealed one (because of the larger CB offset). In fact, our CREM data suggest that electron evacuation under light illumination from the CdSe to the $TiO_2$ is indeed suppressed for the air-annealed sample, a process that should promote increased recombination in contrast to the lifetime data. On the other hand, we also noted the possibility of a more rapid hole injection to the CuSCN for the air-annealed case that will lead to less recombination in the absorber, i.e., longer lifetime. Both the conclusions emerge from the difference in photoinduced Cu and Cd core-level shifts between the air- and nitrogen-annealed samples, as well as by the slight negative charging of the oxidized $CdSeO_4$ surface/interface, detected under light in the CREM experiment. Therefore, combined with the lifetime data, it is likely that the effect of air-annealing to improve hole evacuation from the absorber is much larger than its effect on suppressing the corresponding electron evacuation.

Assuming that the photovoltage decay is a manifestation of recombination of electrons trapped in the $TiO_2$, there are only two pathways for recombination of these electrons: From $TiO_2$ back to the CdSe (pathway 2) and to the CuSCN (pathway 3). (Of course, these will be affected by other pathways; for example, a longer electron lifetime in the CdSe can increase the chance that an electron re-injected into the CdSe conduction band will return to the $TiO_2$, particularly taken together with the enhanced removal of holes from the CdSe to the CuSCN). Considering first back electron injection from the $TiO_2$ into the CuSCN (process 3) one should note that most of the interface in the cell is between $TiO_2$ and CuSCN, because of the poor coverage by

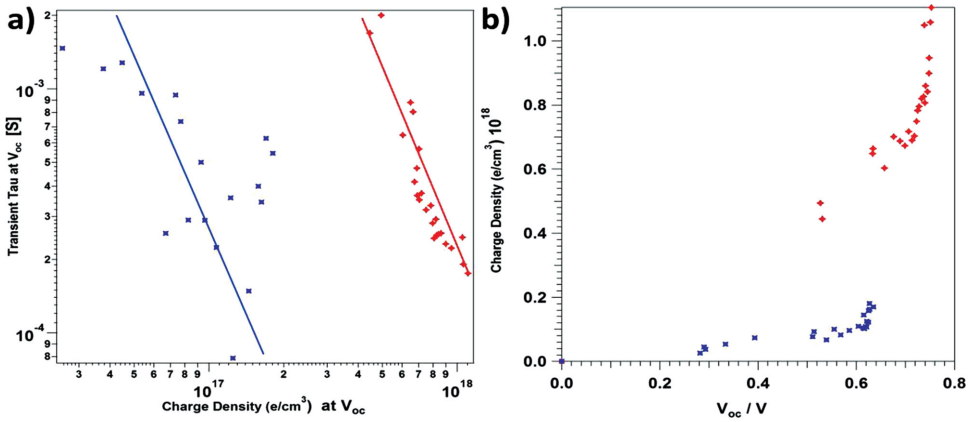


**Figure 7.** a) Charge-carrier lifetime calculated against the charge density of cells fabricated from CdSe annealed at 500 °C in air (red, star shape markers), and under nitrogen (blue, square-shape markers). Each point represents a different light intensity, ranging from 0.01 to 1.7 sun as calibrated using a Si diode. The lines are added only as a guide. b) Charge density, measured at open-circuit, versus $V_{OC}$, for the same cells.

CdSe (Figure 1b). Since high values of $V_{OC}$ are obtained in spite of the preponderance of this interface, it is clearly an efficient blocking interface. The fact that this interface forms a good diode was also shown previously.[38] Therefore, electron injection from the $TiO_2$ to the CuSCN does not seem to be a significant route for recombination (except maybe close to the $V_{OC}$ of the cells using air-annealed CdSe), hence its reduction cannot account for the improvement seen. This leaves path 2, electron injection from $TiO_2$ back to CdSe, as the main pathway for recombination as measured by photovoltage decay. There are a number of reasons why this pathway is expected to be slower for the air-annealed CdSe than for the $N_2$-annealed CdSe: more efficient hole removal from the CdSe to the CuSCN in cells made from air-annealed CdSe discussed earlier and a partially blocking oxidized shell between the CdSe and $TiO_2$ that reduces direct recombination between electrons in the $TiO_2$ and holes in the CdSe, both due to simple blocking as well as to reduced Coulomb attraction between the two charges due to the additional thickness of the shell. From the smaller offset between the CdSe and $TiO_2$ conduction bands for the air-annealed samples, back-electron transfer between the two conduction bands would be expected to be facilitated in the air-annealed sample, but this will again be offset by the CdSe shell-blocking layer.

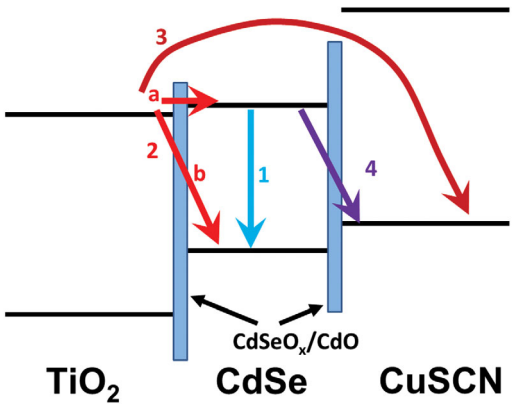


**Scheme 1.** A simplified (absence of trap-mediated processes) energy-band scheme of possible recombination routes in the $TiO_2$/CdSe/CuSCN system. The arrows and numbers represent the different processes (see text). Electrons from $TiO_2$ can return to the CdSe either to holes in the valence band (2b) or to the $TiO_2$ conduction band (2a); in the latter case, recombination can occur by process 1 or 4. These electrons can also move back to the $TiO_2$, in which case recombination does not occur. Process 3 could in principle occur where there is direct contact between the $TiO_2$ and the CuSCN.

We should consider the possibility that some of the stored charge measured in the photovoltage decay originates from sources other than trapped electrons in the $TiO_2$, e.g., trapped electrons in the CdSe shell. Since experimentally, we get a more or less linear plot in Figure 7a, the two mechanisms should necessarily have a comparable time constant that would be somewhat of a coincidence.

We also note electron flow from the CdSe-conduction band to recombine with holes in the CuSCN (process 4, Scheme 1). This pathway can depend on many factors (a possible one is an exchange reaction between the CuSCN, particularly during the CuSCN solution deposition and CdSe, resulting in the formation of Cu–Se species that might act as recombination centers). We have no experimental information on whether or not this pathway occurs or is important.

The increased charge-carrier density as a function of $V_{OC}$ for cells from air-annealed compared with $N_2$-annealed CdSe, shown in Figure 7b, is in full agreement with the longer charge lifetimes in the former. For the dye-sensitized solar cell, where the charge density is normally assumed to come from sub-bandgap traps in the $TiO_2$, two additional mechanisms are also considered to explain the change in charge density:

1. A different trap distribution in different samples: Normally, these traps are considered to be located in the $TiO_2$. However, in our case, we have shown that oxidation causes major changes in trap states at the absorber surfaces and interfaces and the actual role of these trap states in the photovoltage decay data is still an open question.

2. A shift in the $TiO_2$-band edges downward (a larger density of traps); however, based on the band diagrams in Figure 4, the $TiO_2$ does not change appreciably between the air- and $N_2$-annealed samples.

Hence, the overall analysis of charge-dynamics processes suggests that the dominant effect of air-annealing is in passivating hole traps at the CdSe grain-surfaces and, thus, suppressing the dominant role of these sites as recombination centers. A second role of the air-annealing process is observed as well: the formation of a barrier shell and a reduced CBM offset, both acting against electron transport across the CdSe/$TiO_2$ interface. This shell was also found to trap electrons (see $SeO_x$ in Figure 5). In principle, it acts on both electron injection from CdSe to $TiO_2$ as well as on the reverse recombination process 2 in Scheme 1. In particular, the barrier effect is not necessarily symmetrical for electron injection to the $TiO_2$ and back to the CdSe; the latter can potentially promote the improved charge separation observed here. However, as indicated by the CREM data in Figure 5, the steady-state electron density in the illuminated absorber grains effectively increases for the air-annealed, compared with $N_2$-annealed samples. Consequently, (unless marked differences arise in the recombination efficiencies of electrons that originate from direct photogeneration as compared with process 2, Scheme 1), one can conclude that the observed increase in lifetime reflects mainly the charge dynamics in the CdSe and, importantly, that the effect on electron evacuation is of a minor role, as compared with the improvement in hole evacuation.

## 3. Conclusions

We have shown how an oxide layer, usually considered as a blocking barrier against charge transport, turns out to become a $V_{OC}$ enhancer. The formation of an oxidized shell on the CdSe (a) passivates hole traps at the CdSe surfaces and interfaces, and thus efficiently suppresses electron-hole recombination processes and, (b) improves hole evacuation from the CdSe grain. The oxide barrier created at the CdSe grain surfaces does reduce the efficiency of electron transport across the CdSe/$TiO_2$ interface. While this, together with the small conduction-band offset between the CdSe and $TiO_2$, can explain the small values of photocurrent obtained for the cells from air-annealed CdSe, this effect is much less pronounced than the improvement of hole extraction. Thus, the net result is the pronounced increase in charge separation efficiencies and corresponding life-time characteristics, which together lead to the higher $V_{OC}$ observed. The dependence on annealing temperature further suggests tight correlation with the onset for Cd–O appearance and the removal of Se dangling bonds (as well as the pronounced crystal growth). Our conclusions are largely based on an important added value gained by combining CREM and kinetics-oriented methods. In addition to obtaining improved band diagrams, this combination draws direct correlations between mechanisms and their associated cell domains, which as realized here, can frequently become a key piece of information.

## 4. Experimental Section

*Substrate Preparation*: Fluorine-doped tin oxide (FTO, Pilkington, TEC8 8 $\Omega^{-2}$)-coated glass was used as the transparent electrode for the ETA cell. Prior to use, the substrates were cleaned in detergent solution in an ultrasonic bath, rinsed in deionized water, and dried under a $N_2$ stream. A dense $TiO_2$ layer was applied by spin coating a sol–gel solution. For the sol–gel solution, 2.7 mL of titanium (IV) isopropoxide (Sigma–Aldrich) was added to 71 mL of isopropanol and 1.0 g of diethanolamine (Fluka). After mixing for 5 min at room temperature, 70 µL of deionized water was added, and the sol was left to age for an hour. The sol solution was spin-coated on the clean substrates at 4000 rpm for 25 s, followed by annealing. The annealing was carried out in air, by ramping slowly (5 C $min^{-1}$) to 160 C, holding at that temperature for an hour, and then raising the temperature at 5 C $min^{-1}$ to 450 C and maintaining that temperature for another hour. This process was repeated for a total of five times prior to the deposition of the mesoporous layer to obtain an approximately 100-nm-thick-dense $TiO_2$ layer.

Mesoporous $TiO_2$ was spin-coated on top of the dense layer from a suspension made by dispersing 1.0 g of P25 $TiO_2$ nanoparticles (donated by Evonik Industries AG, AEROXIDE $TiO_2$ P25) in 5 mL of ethanol and 1 mL of a 0.02 g $mL^{-1}$ solution of poly(ethylene glycol) (MW: 8000, Fluka) in acetonitrile. The mixture was sonicated for at least 20 min before spin-coating for 25 s at 3000 rpm to yield a 2–3-µm-thick porous electrode. The electrode was then calcined in air using the same heating program as for the dense layer.

*CdSe Deposition*: CdSe was electrodeposited on the electrodes from an aqueous solution of 0.04 M cadmium acetate, 0.1 M potassium trinitriloacetate ($K_3NTA$), and 0.04 M $Na_2SeSO_3$; the pH of the deposition solution was adjusted to 8–8.2 with 4 M KOH. Galvanostatic deposition was performed at 3 mA $cm^{-2}$ cathodic current per geometric substrate area for 3 min. The samples were then rinsed with water, dried under nitrogen flow, and annealed for 30 min under various conditions described in the text.

*CuSCN Deposition and Solar Cell Fabrication*: To complete the photovoltaic device, a CuSCN hole conductor layer and gold contact were deposited on the samples. A saturated solution of CuSCN was prepared by stirring 0.4 g of CuSCN in ca. 13 mL of di-*n*-propylsulfide overnight and allowing it to settle for several days. This solution was diluted with an equal volume of dipropyl sulfide just before use. Prior to CuSCN deposition, the samples were dipped in an aqueous solution of 0.4 M KSCN for 5 min at room temperature and the excess solution was gently wicked off with a Kimwipe tissue. The samples were then placed on a hot plate at 105 °C and the CuSCN deposition was carried out in a homemade apparatus (similar to the one in ref. [39] by using a movable bent syringe needle sealed at the end and with four 0.3-mm diameter holes, spaced 3 mm apart, drilled in the horizontal side of the needle. Typically, 0.4 mL of solution pumped at 40 µL $min^{-1}$ was used for a sample area of 2.5 $cm^2$, resulting in a CuSCN layer ca. 1-µm thick above the $TiO_2$ layer, thus preventing contact between the $TiO_2$ and the Au back contact. Gold contacts, 100-nm thick, were deposited on top of the CuSCN layer by thermal evaporation. A schematic illustration of a full cell structure is shown in Figure 1.

*Characterization*: Optical transmission spectra were measured on a JASCO V570 UV–vis–IR spectrophotometer fitted with an integrating sphere. The measured transmission values were corrected with reflection measurements to obtain reflection-corrected transmission. The morphology of the samples was observed by SEM (Carl Zeiss Leo Ultra 55 scanning electron microscope) using 2 kV accelerating voltage. XRD measurements were conducted on a Rigaku ULTIMA III operated with a copper anode at 40 kV and 40 mA. The measurements were taken using a Bragg–Brentano configuration through a 10-mm slit, a convergence Soller 5° slit, and a nickel filter.

XPS chemical analyses and CREM[33,34] characterization to measure band structures were performed on a slightly modified Kratos Ultra-DLD XPS spectrometer, using a monochromatic Al K$\alpha$ source at 75 W. The work function was measured on the XPS spectrometer both before and after the sample was subjected to X-ray irradiation in order to account for any beam-induced charging effects or irradiation damage. Using a low kinetic-energy electron flood gun (eFG) as a current source, the current at the sample was measured while applying a reverse bias to the sample, starting at elevated values and gradually decreasing the bias. The work function is given by the turning point at which a measurable current

starts to flow. The valence-band edge is extracted from the spectrum after correcting for charging. The conduction-band edge is calculated by adding the optical bandgap to the valence-band edge. CREM-based photovoltage evaluation was provided by applying a halogen source and detecting the various XPS line-shifts, thus following the photovoltages at different domains of the sample, as described previously.[40]

Photovoltaic current–voltage (*I–V*) measurements were performed under AM1.5 100 mW $cm^{-2}$ conditions using a solar simulator (Sciencetech Inc., Canada) and were recorded with a Keithley 2400 source-meter. An area of 1.1 $cm^2$ was defined both by scribing around the gold contact to delineate the cell size and using a mask of the same area.

Transient absorption spectroscopy measurements were recorded by using a Clark-MXR CPA-2010 laser (775 nm fundamental, 150 fs FWHM, 1 kHz repetition rate, and 1 mJ per pulse) and Helios Software supplied by Ultrafast Systems. The pump beam (95% of the fundamental doubled to 387 nm) and probe beam (a white light continuum generated from 5% of the fundamental) are incident on the CdSe–$TiO_2$ samples sealed under vacuum in a 5-mm quartz cell. The pump power was held at 2 mW $cm^{-2}$ and an average of 2000 pump-probe pulses was taken for each delay time.

Photovoltage decay and charge-extraction measurements were done on a home-built device equipped with an array of white LEDs to supply bias light ranging from 1% to 170% sun and red (670 nm) LEDs for the pulse. The system was operated and the data collected and analyzed by using the TRACER software.[39,41] In these measurements, the cell held at open-circuit conditions, is exposed to a bias white light at variable light intensity, and then to an additional perturbation in the form of a red-light pulse of lower intensity. The change in the cell voltage is recorded as a function of time after the end of the light pulse. Then, still under open-circuit conditions, the bias light is turned off and the cell is immediately switched to short-circuit, so that the trapped charges in the cell can be collected. The charge-carrier density can be calculated from the $TiO_2$ thickness.

## Supporting Information

Supporting Information is available from the Wiley Online Library or from the author.

## Acknowledgements

This research was funded by the US–Israel Binational Science Foundation, the Israel Science Foundation, the Leona M. and Harry B. Helmsley Charitable Trust, and the Wolfson Family Trust. The authors are grateful to Dr. Brian O'Regan, Imperial College, London, for his extensive help that enabled us to set up the TRACER system and generously allow the use of the TRACER software. The authors thank Dr. Piers Barnes, Imperial College London, for useful discussions on the photovoltage decay data and Dr. Yaron Tidhar from the Organic Chemistry Department in the Weizmann Institute for help with some of the transient absorption analyses. This is NDRL No. 5028 from Notre Dame Radiation Laboratory, which is supported by the Division of Chemical Sciences, Geosciences, and Biosciences, Office of Basic Energy Sciences of the US Department of Energy through the award DE-FC02–04ER15533.

Received: July 22, 2014
Revised: September 19, 2014
Published online:

[1] P. V. Kamat, K. Tvrdy, D. R. Baker, J. G. Radich, *Chem. Rev.* **2010**, *110*, 6664.
[2] O. Niitsoo, S. K. Sarkar, C. Pejoux, S. Rühle, D. Cahen, G. Hodes, *J. Photochem. Photobiol. Chem.* **2006**, *181*, 306.
[3] G. Hodes, *Phys. Chem. Chem. Phys.* **2007**, *9*, 2181.
[4] H. M. Pathan, B. R. Sankapal, J. D. Desai, C. D. Lokhande, *Mater. Chem. Phys.* **2003**, *78*, 11.
[5] R. B. Kale, S. D. Sartale, B. K. Chougule, C. D. Lokhande, *Semicond. Sci. Technol.* **2004**, *19*, 980.
[6] H. Lee, M. Wang, P. Chen, D. R. Gamelin, S. M. Zakeeruddin, M. Grätzel, M. K. Nazeeruddin, *Nano Lett.* **2009**, *9*, 4221.
[7] M. A. Becker, J. G. Radich, B. A. Bunker, P. V. Kamat, *J. Phys. Chem. Lett.* **2014**, *5*, 1575.
[8] C. Levy-Clement, R. Tena-Zaera, M. A. Ryan, A. Katty, G. Hodes, *Adv. Mater.* **2005**, *17*, 1512.
[9] Y. Golan, L. Margulis, I. Rubinstein, G. Hodes, *Langmuir* **1992**, *8*, 749.
[10] Y. Golan, G. Hodes, I. Rubinstein, *J. Phys. Chem.* **1996**, *100*, 2220.
[11] Y. Yin, A. P. Alivisatos, *Nature* **2005**, *437*, 664.
[12] P. V. Kamat, *J. Phys. Chem. C* **2008**, *112*, 18737.
[13] H. W. Hillhouse, M. C. Beard, *Curr. Opin. Colloid Interface Sci.* **2009**, *14*, 245.
[14] D. Bonnet, E. Rickus, The CdSe thin-film solar cell; Proc. of *the 14th Photovoltaics Specialist Conf.*, **1980**, San Diego, California, 629.
[15] O. Savadogo, K. C. Mandal, *J. Electrochem. Soc.* **1994**, *141*, 2871.
[16] W. U. Huynh, J. J. Dittmer, A. P. Alivisatos, *Science* **2002**, *295*, 2425.
[17] B. Sun, E. Marx, N. C. Greenham, *Nano Lett.* **2003**, *3*, 961.
[18] W. U. Huynh, X. Peng, A. P. Alivisatos, *Adv. Mater.* **1999**, *11*, 923.
[19] J. Liu, T. Tanaka, K. Sivula, A. P. Alivisatos, J. M. J. Fréchet, *J. Am. Chem. Soc.* **2004**, *126*, 6550.
[20] P. Wang, A. Abrusci, H. M. P. Wong, M. Svensson, M. R. Andersson, N. C. Greenham, *Nano Lett.* **2006**, *6*, 1789.
[21] G. Hodes, D. Cahen, *Acc. Chem Res* **2012**, *45*, 705.
[22] I. Barceló, J. M. Campiña, T. Lana-Villarreal, R. Gómez, *Phys. Chem. Chem. Phys.* **2012**, *14*, 5801.
[23] I. Mora-Sero, S. Gimenez, F. Fabregat-Santiago, E. Azaceta, R. Tena-Zaera, J. Bisquert, *Phys. Chem. Chem. Phys.* **2011**, *13*, 7162.
[24] C.-F. Chi, P. Chen, Y.-L. Lee, I.-P. Liu, S.-C. Chou, X.-L. Zhang, U. Bach, *J. Mater. Chem.* **2011**, *21*, 17534.
[25] R. Kniprath, J. P. Rabe, J. T. McLeskeyJr., D. Wang, S. Kirstein, *Thin Solid Films* **2009**, *518*, 295.
[26] G. Hodes, S. J. Fonash, A. Heller, B. Miller, *Adv. Electrochem. Electrochem. Eng.* **1984**, *13*, 113.
[27] A. Heller, G. P. Schwartz, R. G. Vadimsky, S. Menezes, B. Miller, *J. Electrochem. Soc.* **1978**, *125*, 1156.
[28] R. Tenne, G. Hodes, *Appl. Phys. Lett.* **1980**, *37*, 428.
[29] L. Han, D. Qin, X. Jiang, Y. Liu, L. Wang, J. Chen, Y. Cao, *Nanotechnology* **2006**, *17*, 4736.
[30] B. Sun, H. J. Snaith, A. S. Dhoot, S. Westenhoff, N. C. Greenham, *J. Appl. Phys.* **2004**, *97*, 014914.
[31] G. Hodes, E. Grunbaum, Y. Feldman, S. Bastide, C. Levy-Clement, *J. Electrochem. Soc.* **2005**, *152*, G917.
[32] F. Cerdeira, I. Torriani, P. Motisuke, V. Lemos, F. Decker, *Appl. Phys. A* **1988**, *46*, 107.
[33] H. Cohen, *Appl. Phys. Lett.* **2004**, *85*, 1271.
[34] Y. Itzhaik, G. Hodes, H. Cohen, *J. Phys. Chem. Lett.* **2011**, *2*, 2872.
[35] A. Ebina, K. Asano, T. Takahashi, *Phys. Rev. B* **1980**, *22*, 1980.
[36] N. A. Hill, K. B. Whaley, *J. Chem. Phys.* **1994**, *100*, 2831.
[37] C. Burda, S. Link, M. Mohamed, M. El-Sayed, *J. Phys. Chem. B* **2001**, *105*, 12286.
[38] C. Rost, I. Sieber, S. Siebentritt, M. C. Lux-Steiner, R. Könenkamp, *Appl. Phys. Lett.* **1999**, *75*, 692.
[39] B. C. O'Regan, F. Lenzmann, *J. Phys. Chem. B* **2004**, *108*, 4342.
[40] H. Cohen, S. K. Sarkar, G. Hodes, *J. Phys. Chem. B* **2006**, *110*, 25508.
[41] P. R. F. Barnes, K. Miettunen, X. Li, A. Y. Anderson, T. Bessho, M. Gratzel, B. C. O'Regan, *Adv. Mater.* **2013**, *25*, 1881.